

Stochastic Geometry Analysis of EMFE of Idle Users and Network Performance with Dynamic Beamforming

Quentin Gontier, *Graduate Student Member, IEEE*, Charles Wiame, *Member, IEEE*, Joe Wiert, *Senior Member, IEEE*, François Horlin, *Member, IEEE*, Christo Tsigros, Claude Oestges, *Fellow, IEEE*, and Philippe De Doncker, *Member, IEEE*

Abstract—This paper introduces a novel mathematical framework based on stochastic geometry to investigate the electromagnetic field exposure (EMFE) of both active and idle users located at a specific distance from each other, in cellular networks with dynamic beamforming. Accurate modeling of antenna gain, which encompasses both the main and side lobes, becomes crucial in this context. To address this need, the multi-cosine antenna pattern is introduced. The marginal distribution of EMFE for each user type is derived. The paper then examines network performance by introducing a new metric designed to ensure minimal downlink coverage for active users while keeping EMFE for idle users below a specified limit. This metric addresses questions such as, "What is the probability that idle users at a distance of x m from an active user will experience EMFE below a specific limit while the active user meets a particular coverage requirement, and how many antenna elements are needed at the base station to increase this probability of, let us say, 20%?".

Index Terms—Coverage, dynamic beamforming, EMF exposure, Nakagami- m fading, Poisson point process, stochastic geometry.

I. INTRODUCTION

THE rapid evolution of wireless communication technologies has sparked growing concerns about the potential risks associated with electromagnetic field exposure (EMFE) stemming from wireless network infrastructures. Among the effects associated with non-ionizing frequencies, thermal effects stand out as the sole impact unanimously acknowledged within the scientific community [1]. Entities such as the International Commission on Non-Ionizing Radiation Protection (ICNIRP) establish maximal EMFE thresholds based on conservative margins and literature review, specifying basic restrictions in terms of specific absorption rate (SAR) or incident power density (IPD) [2]. Nations or regional entities can then adopt these guidelines or enact more stringent legislation.

This work was supported by Innoviris under the Stochastic Geometry Modeling of Public Exposure to EMF (STOEMP-EMF) grant.

Q. Gontier, F. Horlin and Ph. De Doncker are with Université Libre de Bruxelles, OPERA-WCG, Avenue Roosevelt 50 CP 165/81, 1050 Brussels, Belgium (quentin.gontier@ulb.be).

C. Wiame is with NCRG Group, Massachusetts Institute of Technology, Cambridge, MA 02139 USA.

J. Wiert is with Chaire C2M, LTCI, Télécom Paris, Institut Polytechnique de Paris, 91120 Palaiseau, France.

C. Tsigros is with Department Technologies et Rayonnement, Brussels Environment, Belgium.

C. Oestges is with ICTTEAM Institute, Université Catholique de Louvain, Louvain-la-Neuve, Belgium.

A noteworthy innovation introduced by the 5th generation of cellular networks and subsequent generations is dynamic beamforming (DBF). Using multiple antennas at the base station (BS), DBF enables the formation of narrow beams to mitigate interference. While this significantly enhances the signal-to-interference-plus-noise ratio (SINR), it results in higher EMFE for *active users* (AUs) calling for the beam, compared to *idle users* (IUs) who are not active in the network and who experience lower EMFE on average with shorter exposure times [3]. The distinction in EMFE between AUs and IUs can be leveraged to establish different EMFE constraints for AUs and IUs. This is in line with the desire to establish safe zones called "reduced EMFE areas" for IUs in facilities such as hospitals, schools, or public buildings such as train stations [4]. In this context, investigating the EMFE experienced by IUs is crucial, especially to understand how it varies with the distance from an AU [5]. The IU's EMFE is the sum of the EMFE caused by the BS serving the AU and that caused by interfering BSs. Notably, the shape of the beam plays a pivotal role in influencing IU's EMFE.

The IU's EMFE is intricately linked to the minimal SINR required and the maximum permitted EMFE for AUs, dictating how network operators design their networks. To provide a comprehensive analysis, this paper delves into a study of global network performance by simultaneously examining the EMFE and coverage for AUs, alongside the EMFE experienced by IUs.

The metrics for such an analysis involve random parameters, including network topology, BS beam directions, and propagation channel. To capture this inherent randomness, stochastic geometry (SG) emerges as an efficient tool. Within this framework, BSs are modeled as point processes (PPs), enabling the formulation of network performance in integrals that are both mathematically and computationally tractable.

Motivated by these considerations, the primary aim of this paper is to introduce a comprehensive mathematical framework for marginally and jointly studying network performance. This includes the EMFE for both AUs and IUs and the coverage of AUs, employing an antenna gain model that closely approximates real-world conditions.

A. Related Works

a) *Exploring EMFE*: Numerous studies have evaluated EMFE in 5G and beyond networks. The assessment in 5G is

complex due to heterogeneous networks with macro, small, and femto cells, higher frequencies, and active antennas. The global EMFE is encapsulated by the exposure index (EI) [6], encompassing both uplink (UL) and downlink (DL) EMFE. Compared to previous generations, studies on 5G EMFE fall into field measurements, simulation and mathematical models. A specific DL measurement protocol has been validated in urban environments, calculating time-averaged instantaneous and maximum EMFE for 5G BSs during user calls and idle states [7]. The French spectrum regulator ANFR conducted studies comparing EMFE levels before and after 5G equipment installation, finding similar radiation levels [8]. Another ANFR study using simulations showed higher EMFE for AUs and lower EMFE for IUs in 5G compared to previous generations. Research indicated that narrower beams result in lower EMFE [9]. Comprehensive reviews on the current state of EMFE evaluation for 5G BSs are available in [10] and [11], highlighting the reduction in EMFE levels with the implementation of DBF.

Various strategies have been proposed to further mitigate EMFE levels. For instance, an optimization algorithm introduced in [12] aims to minimize UL and DL EMFE while maintaining quality of service using a small cell network in conjunction with a macro cell network. Another approach employs a smart power control scheme to minimize the EI [13]. Recent advancements explore reconfigurable intelligent surfaces (RIS) to create zones with reduced EMFE while maintaining high data rates, substantiated through ray-tracing simulations [14], [15] and algorithmic optimization of RIS phases [16].

Challenges remain; in-situ measurements provide insights at specific locations under particular conditions, while deterministic numerical evaluations struggle to efficiently capture all sources of randomness within the network.

b) DBF models in SG: SG is a potent tool for computing performance metrics in large networks characterized by various random parameters. BSs are frequently modeled as homogeneous Poisson point processes (PPPs) to balance accuracy and computational tractability. SG has been extensively used to focus on aspects such as SINR and ergodic data rate [17], [18]. Numerous features have been intensively studied, including DBF.

Models of antenna patterns approximate the theoretical distribution of the antenna factor of a Uniform Linear Array (ULA), which is inherently intractable [19], [20]. The sectorized antenna pattern, or flat-top pattern, is the most widely used model. Although it introduces significant discrepancies when calculating performance metrics, it preserves mathematical tractability by assuming a flat gain for the main lobes and a lower gain for the side lobes. The flat-top pattern has found utility in diverse scenarios, including the study of SINR in multi-tier millimeter-wave (mmWave) cellular networks with beamsteering errors [21] and the impact of beam misalignment due to mobility and handovers [22].

An alternative to the flat-top pattern is the cosine approximation of the main lobe of the theoretical ULA pattern, introduced in [20]. This cosine model yields a complementary cumulative distribution function (CCDF) of SINR closer to the one obtained through Monte Carlo simulations based on

the theoretical pattern than the one obtained using the flat-top pattern. It has been applied in various contexts, such as Poisson cluster processes [23] and joint radar communication systems [24].

The Gaussian approximation of the main beam, introduced in [25], has been employed to study the ergodic capacity in mmWave networks with imperfect beam alignment. In comparison to the cosine model, which assumes null gain for the side lobes, the Gaussian model allows for the modeling of side lobes with a constant gain. This advantage proves beneficial for realistic studies on beam misalignment, as demonstrated in [26], where each BS is equipped with three ULAs oriented at 120° intervals, in line with 3GPP specifications.

Finally, an unconventional approach employs a cylindrical array instead of the traditional ULA to study interference, as presented in [27]. This array is modeled as a uniform circular array for the elevation angle and a vertical ULA for the azimuth angle. However, this model lacks tractability and remains largely theoretical.

c) EMFE assessment using SG: In recent years, SG has been instrumental in assessing IPD to optimize it in Wireless Power Transfer (WPT) systems or minimize it for EMF-aware applications. The flat-top model finds widespread application in WPT systems for energy harvesting [28], [29] and for analyzing energy correlation [30]. It has been utilized in works such as [31], [32], where it is employed to estimate simultaneous wireless information and power transfer by computing a joint CCDF to balance coverage and harvested power. Additionally, the Gaussian model is used in [33] to explore the impact of imperfect beam alignment in mmWave WPT systems.

Early works on EMFE assessment within the SG framework are detailed in [34], which employs an empirical propagation model for 5G networks in mmWave scenarios, and in [35], comparing theoretical and experimental EMFE distributions from urban measurements. In [36], EMFE analysis considers max-min fairness power control. The flat-top pattern is used for EMFE analysis in coexisting sub-6 GHz and mmWave networks [37], and in [38], it conducts a joint analysis of EMFE and SINR in β -Ginibre PP and inhomogeneous Poisson PPs. Notably, these two works are the soles that incorporate DBF into the SG model for EMFE. Joint analyses of EMFE and SINR are also conducted in [39] for Manhattan networks, in [40] for user-centric cell-free networks, and in [41] for both UL and DL. An evaluation of EMFE caused by a user's smartphone using SG is presented in [42], where the authors independently study the impact of network parameters on EMFE and signal-to-noise ratio.

However, a notable gap exists in the literature regarding the study of EMFE experienced by an IU in a DBF network, particularly within the SG framework. Additionally, current antenna pattern models struggle to accurately capture the side lobe characteristics, thereby impacting network performance metrics. Preliminary work utilizing the multi-cosine gain pattern is explored in [43] for *random users* in the network, illustrating users not targeted by a beam and lacking proximity information to an AU.

B. Contributions

This paper addresses gaps in the literature by focusing on the evaluation of EMFE for IUs in the SG framework. It introduces a *multi-cosine* antenna gain model, which provides a more accurate representation by accounting for side lobes. The key contributions of this paper are outlined below:

- 1) *EMFE of idle users*: The paper introduces mathematical expressions of the marginal cumulative distribution function (CDF) characterizing any user's EMFE for several literature gain models, compared to the introduced multi-cosine pattern. This model delineate EMFE experienced by AUs and IUs within the network. These mathematical expressions are calculated for several gain models and compared to the introduced multi-cosine pattern.
- 2) *Spatial performance metrics*: The study extends beyond EMFE, encompassing a broader analysis of network performance. This is achieved by jointly computing a spatial CDF that assesses the probability of meeting AU's SINR requirements, while keeping IU's EMFE below a specific limit.

These metrics are investigated as functions of the distance between the AU and the IU, as well as functions of the number of antennas at the BS, providing a comprehensive understanding of the network's performance dynamics.

II. SYSTEM MODEL

A. Topology

Let the two-dimensional spatial domain $\mathcal{B} \in \mathbb{R}^2$ be the network area, defined as a disk with a radius τ and centered at the origin. Within \mathcal{B} , let $\Psi = X_i$ denote the PPP representing the locations of BS X_i , all sharing the same technology, belonging to the same network provider, operating at a carrier frequency f , and being able to transmit at a maximum power P_t . The density of BSs in Ψ is denoted by λ . Each BS is situated at a height $z > 0$ relative to the users. The AU is positioned at the origin and is served by the nearest BS, while all other BSs act as potential interferers. An IU is located at a distance d from the AU and form a random angle Θ_0 with the serving BS, as can be seen from Fig. 1. The distance between the AU and X_i is denoted R_i , the angle formed between the IU and X_i is denoted Θ_i and the distance between the IU and X_i is denoted $P_i = \sqrt{R_i^2 + d^2 - 2R_id \cos(\Theta_i)}$. Additionally, an angle $\delta_i = \text{sign}(\Theta_i) \arccos((R_i - d \cos \Theta_i)/P_i)$ is employed to describe the angle between the AU and the IU from the perspective of X_i . The boresight direction of X_i forms an angle ξ_i with the AU. The serving BS and the associated distances and angles are indexed as 0, with the boresight of X_0 directed towards the AU (i.e., $\xi_0 = 0$). In this configuration, the equipment of the AU is considered with a unitary and isotropic gain. Each BS is equipped with three identical ULAs oriented at 120° intervals, following 3GPP specifications, with each array containing N antennas with half-wavelength spacing. Consequently, the angle ξ_i is a random variable in the interval $[0, 2\pi/3]$. Intracell interference is neglected for simplicity, and an exclusion radius r_e around the users ensures no BS is located within this region. The normalized gain $G(\xi)$ is uniformly scaled by the maximum gain $G_{\max} = N$, and defined

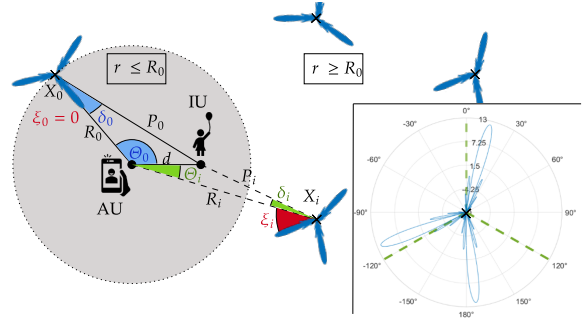


Fig. 1. Scheme of the network with an AU at the origin and an IU at a distance d . The antenna pattern of a typical BS is shown in the lower right corner ($N=16$).

in Subsection II-C. For a conservative approach, the network is considered fully loaded, with each ULA communicating with one AU.

For a PPP, the probability density function (PDF) of R_0 is given by

$$f_{R_0}(r) = \frac{2\pi\lambda r \exp(-\lambda\pi r^2)}{\exp(-\lambda\pi r_e^2) - \exp(-\lambda\pi\tau^2)}. \quad (1)$$

It is essential to note that for the impact of d to be meaningful, the IU must be in the same cell as the AU. Subsequent analyses will, therefore, operate under the assumption that d is smaller than the mean cell radius, defined as $(2\sqrt{\lambda})^{-1}$. In instances where the distance exceeds this threshold, the user will be categorized as a RU, indicating no correlation with the location of the AU, for which expressions are derived in [43]. It is also assumed that $\tau \gg d$.

B. Propagation Model

The propagation model is defined as

$$P_{r,i} = P_t G_i |h_i|^2 l_i \quad (2)$$

where $P_{r,i}$ is the received power from BS X_i , G_i is the BS gain towards the user, $|h_i|^2$ accounts for the fading and l_i is the path loss attenuation. Specifically, $l_i = l(X_i) = \kappa^{-1} (R_i^2 + z^2)^{-\alpha/2}$ for a distance R_i between X_i and the AU, with $\alpha > 2$ the path loss exponent and $\kappa = (4\pi f/c_0)^2$ where c_0 is the speed of light. For the path between X_i and the IU, $\tilde{l}(X_i) = \kappa^{-1} (P_i^2 + z^2)^{-\alpha/2}$. The channel h_i follows a Nakagami- m fading model, making $|h_i|^2$ gamma-distributed with shape parameter m and scale parameter $1/m$. Consequently, the CDF of $|h_i|^2$ is expressed as $F_{|h_i|^2}(x) = \gamma(m, mx)/\Gamma(m)$.

Define $\bar{P}_{r,i} = \bar{P}_r(r_i) = P_t l_i(r_i)$. Let $S_0(0) = \bar{P}_r(r_0) |h_0|^2$ be the useful power received by the AU from X_0 and let $I_0(0) = \sum_{i \in \Psi \setminus \{X_0\}} \bar{P}_{r,i}(r_i) G_i(\xi) |h_i|^2$ be the aggregate interference at the AU's location. Similarly, the signal coming from X_0 and reaching the IU is $S_0(d) = \bar{P}_r(p_0) G(\delta_0) |h_0|^2$ and the aggregate interference at the IU's location is $I_0(d) = \sum_{i \in \Psi \setminus \{X_0\}} \bar{P}_{r,i}(p_i) G_i(\xi + \delta_i) |h_i|^2$. Based on these definitions, the SINR experienced by the AU and conditioned on the distance to the serving BS is given by

$$\text{SINR}_0 = \frac{S_0}{I_0 + \sigma^2} \quad (3)$$

where is the noise power. In the following, the performance metrics will be derived for the user DL power EMFE defined as

$$\mathcal{P} = \sum_{i \in \Psi} \bar{P}_{r,i} G_i |h_i|^2 = S_0 + I_0, \quad (4)$$

which can be converted into a total IPD as, by definition,

$$\mathcal{S} = \sum_{i \in \Psi} \frac{P_t G_i |h_i|^2}{4\pi (r_i^2 + z^2)^{\alpha/2}} = \frac{\kappa}{4\pi} \mathcal{P}. \quad (5)$$

C. Antenna Pattern Models

The various described antenna patterns can be observed in Fig. 2, with a zoom on the first side lobes. The normalized gain of one ULA with N omnidirectional antenna elements and half-wavelength spacing is given by

$$G_{act}(\varphi) = \frac{\sin^2\left(\frac{\pi N}{2} \sin(\varphi)\right)}{N^2 \sin^2\left(\frac{\pi}{2} \sin(\varphi)\right)} \quad (6)$$

where $\varphi \in [-\pi/3, \pi/3]$ and $\varphi = 0$ corresponds to the maximal gain of the main lobe $G_{act}(0) = 1$. While the gain function is closely approximated by a squared cardinal sinus function, this approximation also yields intractable mathematical expressions for calculating performance metrics. Instead, the flat-top antenna pattern is widely used in the literature, and given by

$$G_{ft}(\varphi) = \begin{cases} 1 & \text{if } |\varphi| \leq \varphi_{3dB} \\ g & \text{otherwise} \end{cases} \quad (7)$$

where φ_{3dB} is half of the half-power beamwidth (HPBW) of the actual pattern and g is the side lobes gain chosen.

The cosine antenna pattern [20] approximates the main lobe of the actual pattern while assuming null gain for the side lobes and is expressed as

$$G_{cos}(\varphi) = \begin{cases} \cos^2(N\pi\varphi/4) & \text{if } |\varphi| \leq 2/N \\ 0 & \text{otherwise.} \end{cases} \quad (8)$$

The gaussian approximation is given by

$$G_G(\varphi) = (N - g) \exp(-\eta\varphi^2) + g \quad (9)$$

where $\varphi \in [-\pi/3, \pi/3]$ and $\eta = \ln\left(\frac{N-g}{N/2-g}\right) / \varphi_{3dB}^2$.

Lastly, we introduce the multi-cosine antenna pattern defined as

$$G_{mc}(\varphi) = \begin{cases} \cos^2\left(\frac{N\pi\varphi}{4}\right) & \text{if } |\varphi| \leq 2/N \\ \chi_k \sin^2\left(\frac{N\pi\varphi}{2}\right) & \text{if } \frac{2k}{N} \leq |\varphi| \leq \frac{2k+2}{N} \end{cases} \quad (10)$$

where $\chi_k = \frac{\sin^2(Nx_k)}{N^2 \sin^2(x_k)}$ is the extrema of the k th side lobe of the theoretical gain function, with $0 \leq k \leq k_{\max}$ and $\chi_0 = 1$. The choice of k_{\max} is flexible but should remain below $\lfloor N\sqrt{3}/4 - 1 \rfloor$ to prevent side lobes from extending beyond each ULA's sector. The values of x_k are well approached by the ordered positive solutions of $N \tan(x) = \tan(Nx)$.

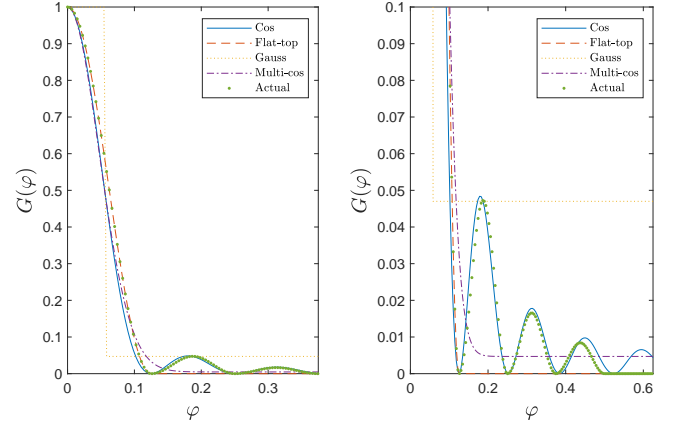


Fig. 2. Antenna patterns for positive angles and zoom ($N=16$)

III. MATHEMATICAL FRAMEWORK

This section is organized as follows: Subsection III-A introduces the preliminary calculations, including moments of the gain and characteristic functions (CFs) of the useful signal and interference, which are essential for the subsequent analysis. Then, Subsection III-B introduces the CDF of EMFE for the different types of users, Subsection III-C reviews the CCDF of SINR of the AU and Subsection III-D provides the joint CDF of the AU's SINR and the IU's EMFE.

A. Preliminaries

In this subsection, the analysis begins with the computation of the central moments of the approximate gain functions for each BS. Each BS is equipped with three identical ULAs, each covering 120° . To mitigate intracell interference, it is assumed that the main beams of two distinct ULAs operating on the same carrier frequency simultaneously cannot be in close proximity. Consequently, it is assumed that the integral of the gain function over 360° can be approximated by three times the integral of the gain function over 120° .

Proposition 1. *The k th moments ($k > 0$) of the approximate gain functions are given by*

$$\mathbb{E}[G_{ft}^k(\varphi)] = \frac{3}{\pi} \varphi_{3dB} (1 - g^k) + g^k; \quad (11)$$

$$\mathbb{E}[G_{cos}^k(\varphi)] = \frac{6 \Gamma(k+1/2)}{N \pi^{3/2} \Gamma(k+1)}; \quad (12)$$

$$\mathbb{E}[G_G^k(\varphi)] = g^k + \frac{3}{2} \sum_{p=1}^k \binom{k}{p} (N-g)^p g^{k-p} \frac{\text{erf}\left(\frac{\pi\sqrt{p\eta}}{3}\right)}{\sqrt{\pi p \eta}}; \quad (13)$$

$$\mathbb{E}[G_{mc}^k(\varphi)] = \frac{6 \Gamma(k+1/2)}{N \pi^{3/2} \Gamma(k+1)} (1 + \chi_{i_{\max}}^\dagger) \quad (14)$$

where $\text{erf}(\cdot)$ is the error function and $\chi_{i_{\max}}^\dagger = \sum_{i=1}^{i_{\max}} \chi_i$.

Proof. The proof is obtained by integrating $\frac{3}{2\pi} \int_{-\pi/3}^{\pi/3} G^2(\varphi) d\varphi$. \square

To derive metrics, whether the coverage of the EMFE, the CF of the useful signal and interference must be calculated at

the AU's and the IU's location. The CF of the useful signal is given in Proposition 2.

Proposition 2. *The CF of the useful signal for the propagation model in (2), from the AU's point of view, conditioned on the distance to the nearest BS R_0 , is*

$$\phi_S(q; 0|R_0) = \mathbb{E}_{S_0} [e^{jqS_0(R_0)}] = (1 - jq\bar{P}_r(R_0)/m)^{-m}. \quad (15)$$

From the IU's point of view, it is given by

$$\begin{aligned} \phi_S(q; d|X_0) &= (1 - jq\bar{P}_r(P_0)G(\delta_0)/m)^{-m} \mathbf{1} [|\delta_0| \leq \pi/3] \\ &\quad + \eta_S(q|X_0)(1 - \mathbf{1} [|\delta_0| \leq \pi/3]). \end{aligned} \quad (16)$$

where $\eta_S(q|X_0)$ depends on the considered gain pattern:

- *Flat-top pattern*

$$\begin{aligned} \eta_S(q|X_0) &= \frac{3\varphi_{3dB}}{\pi} (1 - jq\bar{P}_r(P_0)/m)^{-m} \\ &\quad + \left(1 - \frac{3\varphi_{3dB}}{\pi}\right) (1 - jq\bar{P}_r(P_0)g/m)^{-m} \end{aligned} \quad (17)$$

- *Gaussian pattern*

$$\begin{aligned} \eta_S(q|X_0) &= (1 - jq\bar{P}_r(P_0)g/m)^{-m} \\ &\quad + \sum_{p=1}^{\infty} \frac{3 \operatorname{erf}\left(\frac{\pi\sqrt{p\eta}}{3}\right)}{2\sqrt{\pi p\eta}} (N - g)^p \frac{(jq\bar{P}_r(P_0))^p}{\left(1 - \frac{jq\bar{P}_r(P_0)}{m}\right)^{(m+p)}} \frac{\Gamma(m+p)}{\Gamma(m)m^p p!} \end{aligned} \quad (18)$$

- *Multi-cos pattern*

$$\eta_S(q|X_0) = 1 + \frac{6(1 + \chi_{i\max}^\dagger)}{N\pi} \left({}_2F_1\left(\frac{1}{2}, m; 1; \frac{jq\bar{P}_r(P_0)}{m}\right) - 1 \right) \quad (19)$$

Proof. The proof in (15) is straightforward after applying the expectation operator on $|h|^2$. The proof in (16) is given in Appendix A. \square

The expression of the CF of the interference from the point of view of the IU is assumed to be the same as the one from the point of view of the AU. This is justified by the following observations:

- For the AU as well as for the IU, the orientation of the beam of any interfering BS is random.
- Since $d \ll \tau$, it can be assumed that the disk \mathcal{B} centered on the AU coincides with a disk \mathcal{B}' centered on the IU.
- Since $d \ll (2\sqrt{\lambda})^{-1}$, it is assumed that the AU's closest BS is also the IU's closest BS.

Proposition 3. *The CF of the interference for the propagation model in (2), conditioned on the distance to the nearest BS R_0 , is*

$$\phi_I(q|R_0) = \mathbb{E}_{I_0} [e^{jqI_0}] = \exp(-\pi\lambda\eta_I(q|R_0)) \quad (20)$$

where $\eta_I(q|R_0)$ depends on the considered gain pattern:

- *Flat-top pattern*

$$\begin{aligned} \eta_I(q|R_0) &= \left[r^2 - (r^2 + z^2) \frac{3\varphi_{3dB}}{\pi} {}_2F_1\left(m, -\delta; 1 - \delta; \frac{jq\bar{P}_r(r)}{m}\right) \right]_{r=r_0}^{r=\tau} \\ &\quad - \left[(r^2 + z^2) \left(1 - \frac{3}{\pi}\varphi_{3dB}\right) {}_2F_1\left(m, -\delta; 1 - \delta; \frac{jq\bar{P}_r(r)g}{m}\right) \right]_{r=r_0}^{r=\tau}. \end{aligned} \quad (21)$$

- *Gaussian pattern*

$$\begin{aligned} \eta_I(q|R_0) &= \left[r^2 - (r^2 + z^2) {}_2F_1(-d, m; 1 - d; jq\bar{P}_r(r)g/m) \right. \\ &\quad \left. + \delta (r^2 + z^2) \sum_{p=1}^{\infty} \frac{3 \operatorname{erf}\left(\frac{\pi\sqrt{p\eta}}{3}\right)}{2\sqrt{\pi p\eta}} \left(\frac{N}{g} - 1\right)^p \frac{\Gamma(p+m)}{\Gamma(m)p!} \right. \\ &\quad \left. \times B\left(\frac{jq\bar{P}_r(r)g}{m}; p - \delta, 1 - p - m\right) \left(\frac{jq\bar{P}_r(r)g}{m}\right)^\delta \right]_{r=r_0}^{r=\tau}. \end{aligned} \quad (22)$$

- *Multi-cos pattern*

$$\begin{aligned} \eta_I(q|R_0) &= \frac{3(1 + \chi_{i\max}^\dagger)}{N\pi} \left[(r^2 + z^2) \left(2 - 2 {}_2F_1\left(\frac{1}{2}, m; 1, \frac{jq\bar{P}_r(r)}{m}\right)\right) \right. \\ &\quad \left. + \frac{jq\bar{P}_r(r)}{1 - \delta} {}_3F_2\left(\frac{3}{2}, 1 + m, 1 - \delta; 2, 2 - \delta; \frac{jq\bar{P}_r(r)}{m}\right) \right]_{r=r_0}^{r=\tau} \end{aligned} \quad (23)$$

${}_pF_q(a_1, \dots, a_p; b_1, \dots, b_q; z) = \sum_{n=0}^{\infty} \frac{(a_1)_n \dots (a_p)_n}{(b_1)_n \dots (b_q)_n} \frac{z^n}{n!}$ is the generalized hypergeometric function with $(a)_k = \Gamma(a+k)/\Gamma(a)$ is the Pochhammer symbol. We use the notation $[f(x)]_{x=a}^{x=b} = f(b) - f(a)$.

Proof. The proof is similar to the proof of the Laplace transform of the interference in Lemma 2 and Appendix D in [20]. We recall the main steps with a few changes in Appendix B. \square

B. EMFE

Using the calculations from the previous section, the CDF of the EMFE for the IU or the AU is provided in Theorem 1.

Theorem 1. *The CDF of the EMFE of a user, for the propagation model in (2) in a H-PPP, is given by*

$$\begin{aligned} F_{emfe}^X(T_e) &= \mathbb{P}[\mathcal{P}^X < T_e] \\ &= \frac{1}{2} - \int_{r_e}^{\tau} \int_0^{\infty} \frac{1}{\pi q} \operatorname{Im}[\phi_E^X(q; d|r_0) e^{-jqT_e}] dq f_R(r_0) dr_0. \end{aligned}$$

where X is either the AU with $\phi_E^{AU}(q|r_0) = \phi_S(q; 0|r_0)\phi_I(q|r_0)$ or the IU with $\phi_E^{IU}(q|r_0) = \frac{1}{2\pi} \int_0^{2\pi} \phi_S(q; d|r_0, \theta) d\theta \phi_I(q|r_0)$. The EMFE limit is denoted T_e .

Proof. The result follows from the Gil-Pelaez theorem [44]. \square

It is worth noting that the CDF of EMFE for a random user (RU) is given by setting $\phi_E^{RU}(q; d|r_0) = \phi_I(q|r_e)$ in Theorem 1. The expression of the CF of interference differs from that in [43] due to the methodological approach. While [43] follows the classical method, applying the expectation operators over ξ_i and h_i first, and then over r_i , the method used in this paper, inspired by [20], first applies the operator over r_i and then over the others. This latter approach offers the advantage of easier generalization to various gain and fading models, leveraging knowledge of the moments of $G(\xi)$ and $|h|^2$.

C. Coverage

The CCDF of the SINR is now a textbook development. It has been derived for models with various features, including DBF with the various described antenna pattern. The difference in this paper resides in the CFs of the signal and

interference, whose expression was given in Subsection III-A. It is therefore given as such in Lemma 1.

Lemma 1. *The CCDF of the SINR, for the propagation model in (2) in a H-PPP, is given by*

$$F_{cov}(T_c) \triangleq \mathbb{E}_0 [\mathbb{P}[\text{SINR}_0 > T_c]] \\ = \int_{r_0} \left(\frac{1}{2} + \int_0^\infty \text{Im}[\phi_{\text{SINR}}(q, T_c | r_0)] \frac{1}{\pi q} dq \right) f_{R_0}(r_0) dr_0$$

where $\phi_{\text{SINR}}(q, T_c | r_0) = \phi_S(q; 0 | r_0) \phi_I(-T_c q | r_0) e^{-jT_c q \sigma^2}$ and T_c is the SINR threshold.

D. Joint Spatial Metric

In this subsection, the spatial CDF jointly analyzing the SINR experienced by the AU and the EMFE experienced by the IU is calculated and given in Theorem 2. The conditional CDF and bounds are then provided.

Theorem 2. *The joint CDF of the SINR of the AU and the EMFE of the IU, the two users being separated by a distance d , for the propagation model in (2) in a H-PPP, is*

$$\mathcal{J}(T_c, T_e; d) = \mathbb{E}_0 [\mathbb{P}[\text{SINR}_0 > T_c, \mathcal{P}(d) < T_e]] \\ = \frac{-1}{4} + \frac{1}{2} F_{cov}(T_c) + \frac{1}{2} F_{emfe}(T_e) - \frac{1}{\pi^2} \Upsilon(T_c, T_e; d) \quad (24)$$

where

$$\Upsilon(T_c, T_e; d) = \frac{1}{2\pi} \int_0^\tau \int_0^{2\pi} \Upsilon(T_c, T_e; d | r_0, \theta_0) d\theta f_{R_0}(r_0) dr_0, \\ \Upsilon(T_c, T_e; d | r_0, \theta_0) = \int_0^\infty \int_0^\infty \frac{\epsilon(q, q'; T_c, T_e, d | r_0, \theta_0)}{q q'} dq dq', \\ \epsilon(q, q'; T_c, T_e, d | r_0, \theta_0) \\ = \frac{1}{2} \text{Re} [\epsilon_+(q, q'; T_c, T_e, d | r_0, \theta_0) - \epsilon_-(q, q'; T_c, T_e, d | r_0, \theta_0)], \\ \epsilon_\pm(q, q'; T_c, T_e, d | r_0, \theta_0) \\ = \gamma_\pm(-q T_c, q' | r_0) \phi_S(q; 0 | \Psi) \phi_S(\pm q'; d | \Psi) e^{-j(q T_c \sigma^2 \pm q' T_e)}$$

(25)

and $\gamma_\pm(q, q' | r_0)$ is given in (26) at the top of the next page.

Proof. The proof is provided in Appendix C. \square

For the ease of analysis, we propose in Lemma 2 the conditional joint CDF of the AU's SINR and IU's EMFE, conditioned on the AU's SINR. This is particularly useful for legislators to observe the impact of a more stringent EMFE limit on the network performance.

Lemma 2. *The joint CDF of the AU's SINR and IU's EMFE, conditioned on the AU's SINR is*

$$\mathcal{H}(T_e | T_c; d) = \frac{\mathcal{J}(T_c, T_e; d)}{F_{cov}(T_c)}. \quad (27)$$

Proof. This metric is obtained from Bayes' rule. \square

Due to the intricate nature of the equations, the analytical computation of $\mathcal{J}(T_c, T_e; d)$ can be time-consuming. To address this, an efficient solution is to determine the Fréchet lower bound (FLB) and the Fréchet upper bound (FUB), which are given in Lemma 3.

Lemma 3. *The expression of $\mathcal{J}(T_c, T_e; d)$ in Theorem 2 is bounded by the Fréchet bounds*

$$FLB = \max(0, F_{cov}(T_c^u) + F_{emfe}^{IU}(T_e) - 1) \quad (28)$$

and

$$FUB = \min(F_{cov}(T_c^u), F_{emfe}^{IU}(T_e)) \quad (29)$$

such that $FLB \leq \mathcal{J}(T_c, T_e; d) \leq FUB$.

Lemma 3 can easily be adapted to obtain bounds on the conditional CDF (27) by dividing all members of the inequality by $F_{cov}(T_c)$.

IV. NUMERICAL RESULTS

In this section, the metrics derived in Section III are analyzed using the values of network parameters listed in Table IV. The bandwidth of 20 MHz is a typical value for the 3.5 GHz frequency band. Based on propagation models used in similar cellular networks [35], [45], we set the path loss exponent to $\alpha = 3.2$. The noise power is $\sigma^2 = 10 \log_{10}(k T_0 B_w) + 30 + \mathcal{F}_{dB}$ in dBm where k is the Boltzmann constant, T_0 is the standard temperature (290 K), B_w is the bandwidth and $\mathcal{F}_{dB} = 6$ dB is the receiver noise figure [46]. The value of k_{\max} was chosen to model a sufficient number of side lobes. Beyond this number, the side lobe power drops below one thousand of the main lobe power, and the lobes no longer align with those of the actual pattern.

TABLE I
SIMULATION PARAMETERS

f	3.5 GHz	τ	3 km
B_w	20 MHz	z	30 m
r_e	0.3 m	P	48 dBm
λ	10 BS/km ²	N	64
σ^2	-95.40 dBm	α	3.25
k_{\max}	10		

A. Marginal Distributions of EMFE and SINR

The marginal distribution of EMFE for an IU located 10 m from the AU with $N = 64$ is illustrated in Fig. 3 for the different antenna patterns introduced in Subsection II-C. The proximity of the CDFs for the actual and multi-cosine antenna patterns, in contrast to those for other antenna patterns, underscores the significance of the newly introduced antenna pattern. Utilizing conventional antenna patterns from the literature, such as flat-top or cosine, results in absolute errors of 19% and 33%, respectively, compared to a 1% error with the multi-cosine pattern. The multi-cosine antenna pattern slightly overestimates EMFE, aligning with a conservative approach, which is preferable to underestimation. The CDF of EMFE for the AU (equivalent to $d = 0$ m) is also depicted, with only one CDF shown for the AU. This is because the primary contribution to EMFE comes from the main lobe of its serving BS, unaffected by the chosen gain model. Additionally, Fig. 3 presents the CDF of EMFE for a RU located randomly within the network, without knowledge of its distance from an AU, as analyzed in [43]. This demonstrates that lack of knowledge regarding user location can significantly underestimate EMFE.

$$\begin{aligned}
\gamma_{\pm}(q, q' | r_0) = & \exp\left(\frac{12\lambda}{N}\left[(1+k_{\max})\left(\frac{3(1+k_{\max})}{N\pi} - 1\right)r^2\right.\right. \\
& - \sum_{k=0}^{k_{\max}} \sum_{l=0}^{m-1} \binom{-1/2}{l} \binom{m-1}{l} \left(\frac{6}{N\pi} \sum_{p=0}^{k_{\max}} \sum_{l'=0}^{m-1} \binom{-1/2}{l'} \binom{m-1}{l'} \frac{r^{2+\alpha(2m-1)} F_1\left(2m-1-l-l'+\frac{2}{\alpha}, \frac{2m-1}{2}, \frac{2m-1}{2}, 2m-l-l'+\frac{2}{\alpha}, \frac{-jm}{q\chi_k \bar{P}_r(r)}, \frac{\mp jm}{q'\chi_k \bar{P}_r(r)}\right)}{(2+\alpha(2m-1-l-l'))(jq\chi_k \bar{P}_r(r)/m)^{m-l-\frac{1}{2}}(\pm jq'\chi_k \bar{P}_r(r)/m)^{m-l'-\frac{1}{2}}}\right. \\
& \left. \left. + \frac{2(r^2+z^2)\left(1-\frac{6(1+k_{\max})}{N\pi}\right)}{(4+\alpha(2m-2l-1))} \left(\frac{{}_2F_1\left(1, 1-l+\frac{2}{\alpha}; \frac{1}{2}-l+m+\frac{2}{\alpha}; \frac{-jm}{q\chi_k \bar{P}_r(r)}\right)}{(jq\chi_k \bar{P}_r(r)/m)^{1-l}(1-jq\chi_k \bar{P}_r(r)/m)^{m-\frac{3}{2}}} + \frac{{}_2F_1\left(1, 1-l+\frac{2}{\alpha}; \frac{1}{2}-l+m+\frac{2}{\alpha}; \frac{\mp jm}{q'\chi_k \bar{P}_r(r)}\right)}{(\pm jq'\chi_k \bar{P}_r(r)/m)^{1-l}(1\mp jq'\chi_k \bar{P}_r(r)/m)^{m-\frac{3}{2}}}\right)\right] \Bigg|_{r=r_0}^{r=\tau} \quad (26)
\end{aligned}$$

Markers in the figure represent numerical values obtained from Theorem ??, while solid lines are derived from Monte Carlo simulations (MCSs). The close alignment between these results validates the mathematical model.

The CDF of the IU's EMFE is showed again with a solid line in Fig. 4 along with its detailed contributions. The CDF of the signal power from the AU's serving BS is represented by a dashed line, while the CDF of the interference power from all other BSs is depicted with a dash-dotted line. It can be observed that high EMFE values experienced by the IU primarily originate from the main lobe of the AU's serving BS. However, when the IU is not illuminated by this main lobe, the main contribution to its EMFE does not necessarily come from the side lobes of the interfering BS. This is evident because the CDF of signal power and total EMFE are not close for low EMFE values. Instead, the main lobes of other neighboring BSs contribute significantly, with side lobes of interfering BSs contributing to a lesser extent. This indicates that assessing EMFE solely from the main lobe of the closest BS is insufficient for a comprehensive characterization of EMFE. These observations are highly dependent on the values of N and d , which are analyzed in Subsection IV-C.

Finally, the CCDF of SINR obtained in Lemma 1 is illustrated in Fig. 5 for different antenna patterns, for $N = 64$ and $d = 10$ m. The impact of the gain model choice, while noticeable, is less significant for SINR than for EMFE. This explains the previous lack of demand for a more accurate model. The multi-cosine model results in an absolute error of less than 1%, whereas the flat-top and cosine models show errors of 5% and 8%, respectively. It is also noteworthy that, although the useful signal from the serving BS is much stronger than the interference, the situation is not noise-limited. This is evident when comparing the CCDFs of SINR and SNR.

B. Joint and Conditional Distributions of EMFE and SINR

The conditional CDF of AU's SINR and IU's EMFE is depicted in Fig. 6 for different values of T_e and d , considering an AU's SINR of at least 11 dB and $N = 64$. Markers are derived from Lemma 2 while solid lines are obtained from MCSs. The proximity between the curves proves the validity of the mathematical expressions. Dash-dotted lines and dashed lines represent the FLB and FUB, respectively. The Fréchet bounds provide an accurate approximation of the conditional CDF, appearing closer to the FUB for low EMFE limits and nearer to the FLB for high EMFE limits. It is observed that

\mathcal{H} increases slowly when $T_e = -70$ dBm as d increases, while it rises rapidly for higher EMFE limits. This can be attributed to the fact that, for large EMFE limits, there is a higher probability that the main lobe of the AU's serving BS is the primary factor preventing the IU from staying below the limit as it moves away. The probability that the main lobe of the AU's serving BS is the primary source of EMFE is shown by the dotted line in Fig. 6, delineating the zone of influence of this lobe. At a distance of 10 m from the AU, this probability already drops to 15%. Consequently, at this distance, for $T_e = -60$ dBm or higher limits, \mathcal{H} exceeds 64% while it is only 16% for $T_e = -60$ dBm. This indicates that not only the main lobe of the AU's serving BS but also the side lobes and the gain of other BSs prevent the IU's EMFE from falling below the limit. The conditional probability continues to rise as the IU moves away from the AU but eventually reaches a threshold. This threshold is attained more quickly for high EMFE limits compared to low ones. For $T_e = -70$ dBm, this occurs around 60 m. At this distance, the probability that the EMFE caused by the main lobe of the AU's serving BS is dominant is approximately 2%.

C. Impact of parameters N and d

The parameters N and d significantly influence the EMFE experienced by the IU, directly impacting the main lobe's width and the side lobes' height and width. Fig. 7 illustrates the probability $F_{\text{emfe}}(T_e) = x$ for fixed values of T_e and x , across various values of d and N , with N expressed as powers of 2. For example, consider $F_{\text{emfe}}(-50 \text{ dBm}) = 0.5$. The contour plot indicates the pair of parameters (d, N) where the median IU's EMFE is -50 dBm. When the IU is very close to the AU, the main lobe should exhibit a highly directive beam. At 1 m, N must exceed 90. At 10 m, $N = 16$ is enough and $N = 8$ is adequate at 20 m. If the EMFE limit is 10 dBm stricter, N needs to be increased by a factor 4. Although these values of N appear high, it is important to note the use of very strict limits for this analysis. According to the relationships in [38], $T_e = -60$ dBm corresponds to $171 \mu\text{W}/\text{m}^2$ or $25 \text{ mV}/\text{m}$, to be compared to the international recommendation of ICNIRP of $10 \text{ W}/\text{m}^2$ [2].

A similar analysis can be performed for the joint CDF of the AU's SINR AU and IU's EMFE, as depicted in Fig. 8 for various values of T_e , with $T_e = 11$ dB. Consider a potential future scenario that network providers might need to adhere to. For instance, suppose network providers must ensure that the EMFE of IUs located 2 m from an AU remains below -50 dBm

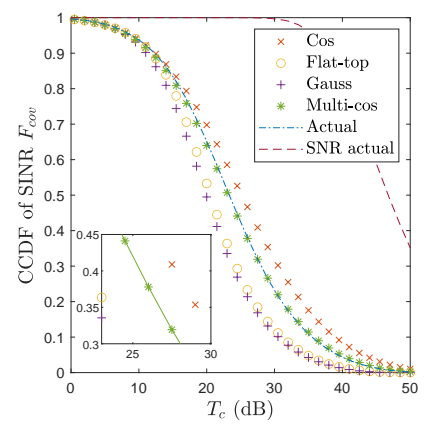
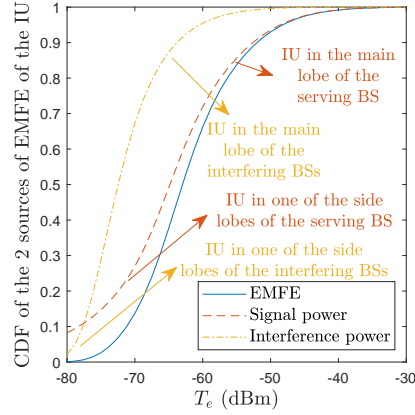
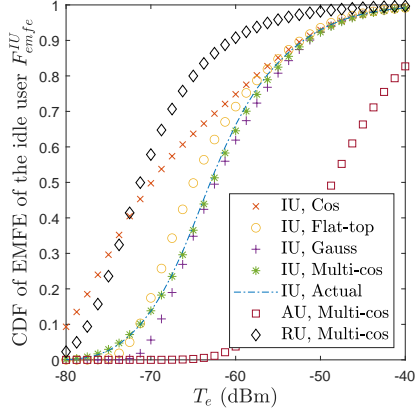


Fig. 3. CDF of EMFE of the IU for different antenna patterns and of the RU for the actual contributing to the total IU's EMFE. $N = 64$, $d = 10$ m.

Fig. 4. CDF of signal and interference power contributing to the total IU's EMFE. $N = 64$, $d = 10$ m.

Fig. 5. CCDF of SINR for different antenna patterns and zoom on the CCDF. $N = 64$, $d = 10$ m.

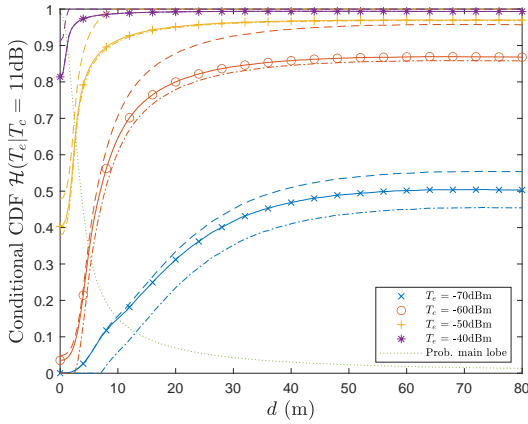


Fig. 6. Conditional CDF of AU's SINR and IU's EMFE when the AU's SINR is at least 11 dB and $N = 64$. Markers are obtained from Lemma 2 and solid lines from MCSs. The dash-dotted lines and dashed lines represent the FLB and FUB, respectively.

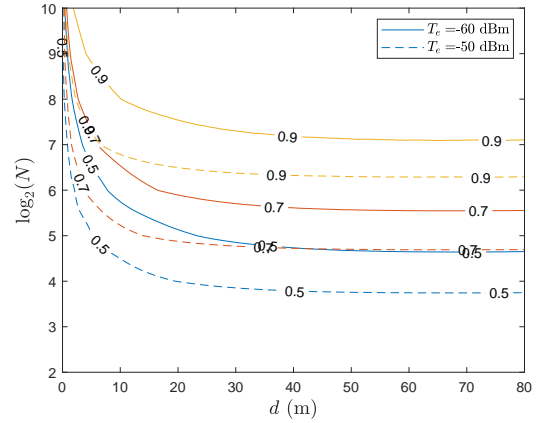


Fig. 8. Contour plot of the joint CDF of the IU's EMFE and the AU's SINR for various values of N , d and T_e , with $T_c = 11$ dB

at least 90% of the time, while also maintaining the AU's SINR above 11 dB. According to Fig. 8, this requirement can be met by employing directive antennas with at least 256 elements.

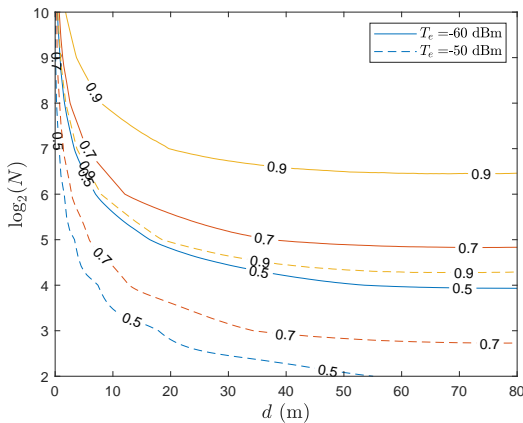


Fig. 7. Contour plot of the CDF of the IU's EMFE for various values of N , d and T_e

V. CONCLUSION

In this paper, a marginal and joint analysis of the EMFE of an IU and the coverage experienced by an AU, located at a specific distance from the IU, was conducted. Due to the absence of sufficiently accurate and tractable antenna pattern models in the literature, a new model, the multi-cosine model, was introduced. This model closely approximates the actual antenna pattern. The model presented in this paper addresses various questions regarding the IU's EMFE as a function of the number of antenna elements at the BS and the distance to the closest AU. The analysis demonstrates that when $N = 64$, the presence of an AU has, on average, no significant impact on the IU's EMFE beyond 60 m. It was determined that N should exceed 256 to ensure a 90% probability that the AU's SINR remains above 11 dB while the IU's EMFE stays below -50 dBm when they are 2 m apart.

APPENDIX A

PROOF OF THE CF OF THE USEFUL SIGNAL SEEN FROM THE IU

If the angle δ_0 is larger than 60° , the AU and the IU are not located in the same sector. The beam of the serving BS launched towards the AU has therefore no impact on the IU's EMFE. The CF of the useful signal from the point of view of the IU, conditioned on the distance location of the serving BS, should therefore consider these two cases in its definition:

$$\begin{aligned} \phi_S(q; d|X_0) &= \mathbb{E}_{|h|} \left[e^{jq\bar{P}_r(P_0)G(\delta_0)|h|^2} \mathbb{1} [|\delta_0| \leq \pi/3] \right] \\ &+ \mathbb{E}_{|h|, \xi} \left[e^{jq\bar{P}_r(P_0)G(\xi)|h|^2} \mathbb{1} [|\delta_0| > \pi/3] \right]. \end{aligned} \quad (30)$$

where $\mathbb{1}[\cdot]$ is the indicator function. Applying the expectation operator $\mathbb{E}_{|h|}[\cdot]$ on the term for the case $\mathbb{1} [|\delta_0| \leq \pi/3]$, we obtain

$$\mathbb{E}_{|h|} \left[e^{jq\bar{P}_r(P_0)G(\delta_0)|h|^2} \right] = (1 - jq\bar{P}_r(P_0)G(\delta_0)/m)^{-m}. \quad (31)$$

For the term with the case $\mathbb{1} [|\delta_0| > \pi/3] = 1 - \mathbb{1} [|\delta_0| \leq \pi/3]$, let us develop the Taylor series of the exponential function. Then, the infinite sum and the expectation operators can be swapped. Knowing that $\mathbb{E}_{|h|} [|h|^{2k}] = \frac{\Gamma(m+k)}{\Gamma(m)m^k}$, using the notation $z = jq\bar{P}_r(P_0)$, we have

$$\begin{aligned} \mathbb{E}_{|h|, \xi} \left[e^{zG(\xi)|h|^2} \right] &= \mathbb{E}_{|h|, \xi} \left[\sum_{k=0}^{\infty} \frac{(zG(\xi)|h|^2)^k}{k!} \right] \\ &= 1 + \sum_{k=1}^{\infty} \frac{z^k}{k!} \mathbb{E}_{\xi} [G^k(\xi)] \frac{\Gamma(m+k)}{\Gamma(m)m^k} := \eta_S(q|X_0). \end{aligned} \quad (32)$$

(16) is then obtained by inserting (31) and (32) in (30). Then $\eta_S(q|X_0)$ can be developed separately for each gain function, using Proposition 1:

- (17) is obtained by inversely applying the definition of the binomial series.
- (19) is obtained by inversely applying the definition of the series expansion of the hypergeometric function ${}_2F_1(\cdot; \cdot; \cdot)$.
- The case of the Gaussian pattern is more complex. In that case, using (13), $\eta_S(q|X_0)$ is given by

$$\begin{aligned} \eta_S(q|X_0) &= \sum_{k=0}^{\infty} \binom{zg}{m}^k \frac{\Gamma(m+k)}{\Gamma(m)k!} \\ &+ \sum_{k=1}^{\infty} \frac{3}{2} \frac{z^k}{k!} \frac{\Gamma(m+k)}{\Gamma(m)m^k} \sum_{p=1}^k \binom{k}{p} (N-g)^p g^{k-p} \frac{\operatorname{erf}\left(\frac{\pi\sqrt{p\eta}}{3}\right)}{\sqrt{\pi p\eta}} \end{aligned} \quad (33)$$

The first term in (33) is solved by inversely applying the definition of the binomial series. The second term can be rewritten as

$$\begin{aligned} &\sum_{p=1}^{\infty} \frac{3 \operatorname{erf}\left(\frac{\pi\sqrt{p\eta}}{3}\right)}{2\sqrt{\pi p\eta}} (N-g)^p \sum_{k=p}^{\infty} \frac{z^k}{k!} \frac{\Gamma(m+k)}{\Gamma(m)m^k} \binom{k}{p} g^{k-p} \\ &= \sum_{p=1}^{\infty} \frac{3 \operatorname{erf}\left(\frac{\pi\sqrt{p\eta}}{3}\right)}{2\sqrt{\pi p\eta}} (N-g)^p \frac{z^p}{p!} \frac{\Gamma(m+p)}{\Gamma(m)m^p} \left(1 - \frac{z}{m}\right)^{-(m+p)} \end{aligned} \quad (34)$$

Replacing (34) in (33) gives (18) in Proposition 2.

APPENDIX B

PROOF OF PROPOSITION 3

The CF function of the interference of the AU at the origin is defined and commonly written as $\phi_I(q|r_0) = \mathbb{E}_{I_0} [\exp(jqI_0(0))]$. Following from [20], and contrarily to the conventional procedure, the first step consists of taking first the expectation over the interferers' locations, by means of the probability generating functional:

$$\begin{aligned} \phi_I(q|R_0) &= \mathbb{E}_{I_0} [e^{jqI_0(0)}] \\ &= \exp \left(-\pi\lambda \mathbb{E}_{\xi, |h|} \left[2 \int_{R_0}^{\tau} (1 - e^{jqP_r(r)}) r dr \right] \right) \\ &= \exp \left(-\pi\lambda \left(\underbrace{\tau^2 - R_0^2 - \mathbb{E}_{\xi, |h|} \left[\int_{R_0}^{\tau} 2e^{jqP_r(r)} r dr \right]}_{\eta_I(q|R_0)} \right) \right). \end{aligned} \quad (35)$$

By using the change of variable $t \rightarrow -jqP_r(r)$ and writing $\delta = 2/\alpha$, the integral can be rewritten

$$\begin{aligned} &\int_{R_0}^{\tau} 2e^{jqP_r(r)} r dr \\ &= \delta \int_{-jqP_r(R_0)}^{-jqP_r(\tau)} (jqP_t \kappa^{-1} G|h|^2)^{\delta} e^{-t} (-t)^{-1-\delta} dt \\ &= \delta (-jqP_t \kappa^{-1} G|h|^2)^{\delta} [\Gamma(-\delta, -jqP_r(r))]_{r=R_0}^{r=\tau}. \end{aligned} \quad (36)$$

$\Gamma(a, z)$ is the upper incomplete Gamma function whose definition and expansion series are [47]

$$\Gamma(a, z) = \int_z^{\infty} e^{-t} t^{a-1} dt = \Gamma(a) - \sum_{k=0}^{\infty} \frac{(-1)^k z^{a+k}}{k!(a+k)}. \quad (37)$$

Using this expansion series in (36) and inserting it in $\eta_I(q|R_0)$ in (35) and letting $\Xi(r) = jq\bar{P}_r(r)$ gives

$$\eta_I(q|R_0) = \left[r^2 + \delta \left(\tau^2 + z^2 \right) \sum_{k=0}^{\infty} \frac{\Xi^k(r) \mathbb{E}_{\xi, |h|} [G^k |h|^{2k}]}{k!(k-\delta)} \right]_{r=R_0}^{r=\tau}.$$

Extracting the terms $k=0$ and using $\mathbb{E} [|h|^{2k}] = \frac{\Gamma(m+k)}{\Gamma(m)m^k}$, gives after some simplifications

$$\eta_I(q|R_0) = \delta \left[\left(r^2 + z^2 \right) \sum_{k=1}^{\infty} \frac{\mathbb{E}_{\xi} [G^k(\xi)] \Xi^k(r) \Gamma(m+k)}{k!(k-\delta) \Gamma(m)m^k} \right]_{r=R_0}^{r=\tau}. \quad (38)$$

Similarly to what is done for $\eta_S(q|X_0)$ in Appendix A, $\eta_I(q|R_0)$ can be developed separately for each gain function, using Proposition 1. The expressions of $\eta_I(q|R_0)$ for the flat-top and multi-cos patterns in Proposition 3 are obtained by using the series expansion of the generalized hypergeometric function ${}_pF_q(\cdot; \cdot)$. For case of the Gaussian pattern is again more complex. Using (13) and writing $\eta_I(q|r)$ such that $\eta_I(q|R_0) = [\eta_I(q|r)]_{r=R_0}^{r=\tau}$, we have

$$\begin{aligned} \eta_I(q|r) &= \delta \left(r^2 + z^2 \right) \sum_{k=0}^{\infty} \left(\frac{\Xi(r)g}{m} \right)^k \frac{\Gamma(m+k)}{\Gamma(m)k!(k-\delta)} + r^2 + z^2 \\ &+ \sum_{k=1}^{\infty} \frac{3}{2} \frac{\Xi^k(r) \delta \left(r^2 + z^2 \right) \Gamma(m+k)}{\Gamma(m)m^k (k-\delta)k!} \sum_{p=1}^k \binom{k}{p} (N-g)^p g^{k-p} \frac{\operatorname{erf}\left(\frac{\pi\sqrt{p\eta}}{3}\right)}{\sqrt{\pi p\eta}} \end{aligned} \quad (39)$$

The first term in (39) is solved by inversely applying the series expansion of ${}_2F_1(\cdot; \cdot; \cdot)$:

$$\sum_{k=0}^{\infty} \left(\frac{\chi g}{m}\right)^k \frac{\Gamma(m+k)}{\Gamma(m)k!(k-\delta)} = -\frac{1}{\delta} {}_2F_1(-\delta, m; 1-\delta; \frac{\chi g}{m}).$$

Introducing the generalized beta function $B(\cdot; \cdot, \cdot)$, the term of the second line in (39) can be rewritten as

$$\begin{aligned} & \sum_{p=1}^{\infty} \frac{3 \operatorname{erf}\left(\frac{\pi\sqrt{p\eta}}{3}\right)}{2\sqrt{\pi p\eta}} (N-g)^p \sum_{k=p}^{\infty} \frac{z^k}{k!} \frac{\Gamma(m+k)}{\Gamma(m)m^k(k-\delta)} \binom{k}{p} g^{k-p} \\ &= \sum_{p=1}^{\infty} \frac{3 \operatorname{erf}\left(\frac{\pi\sqrt{p\eta}}{3}\right)}{2\sqrt{\pi p\eta}} \left(\frac{N}{g} - 1\right)^p \frac{\Gamma(p+m)}{\Gamma(m)p!} \\ & \quad \times B\left(\frac{gz}{m}; p-\delta, -p+1-m\right) \left(\frac{gz}{m}\right)^\delta. \end{aligned} \quad (40)$$

APPENDIX C PROOF OF THEOREM 2

A. General Form of the Metric

The fading coefficients affecting the links related to the two locations being independent, conditioned on the PP Ψ , the joint metric can be decomposed as $\mathcal{J}(T_c, T_e; d) = \mathbb{E}_{\Psi} [\mathbb{P}[\text{SINR}_0 > T_c | \Psi] \mathbb{P}[\mathcal{P}^{IU}(d) < T_e | \Psi]]$. The two factors in the above product can be developed using the Gil-Pelaez theorem. Using again the assumption of a CF of the interference identical for the AU and the IU, let $\phi_{\text{SINR}}(q, T_c | \Psi) = \phi_S(q; 0 | \Psi) \phi_I(-qT_c | \Psi) e^{-jqT_c\sigma^2}$ and $\phi_E^{IU}(q; d | \Psi) = \phi_S(q; d | \Psi) \phi_I(q | \Psi) e^{-jqT_e}$ be respectively the CFs of the signal and interference conditioned on Ψ . Using these notations, we get

$$\begin{aligned} \mathcal{J}(T_c, T_e; d) &= \mathbb{E}_{\Psi} \left[\left(\frac{1}{2} + \int_0^{\infty} \operatorname{Im}[\phi_{\text{SINR}}(q, T_c | \Psi)] \frac{1}{\pi q} dq \right) \right. \\ & \quad \left. \left(\frac{1}{2} - \int_0^{\infty} \operatorname{Im}[\phi_E^{IU}(q'; d | \Psi) e^{-jq'T_e}] \frac{1}{\pi q'} dq' \right) \right]. \end{aligned}$$

By distributing the terms then the expectation operator, we get

$$\begin{aligned} \mathcal{J}(T_c, T_e; d) &= -\frac{1}{4} + \frac{1}{2} \mathbb{E}_{\Psi} \left[\underbrace{\frac{1}{2} + \int_0^{\infty} \operatorname{Im}[\phi_{\text{SINR}}(q, T_c | \Psi)] \frac{1}{\pi q} dq}_{F_{\text{cov}}(T_c | \Psi)} \right. \\ & \quad \left. + \frac{1}{2} \mathbb{E}_{\Psi} \left[\frac{1}{2} - \int_0^{\infty} \operatorname{Im}[\phi_E^{IU}(q'; d | \Psi) e^{-jq'T_e}] \frac{1}{\pi q'} dq' \right] \right] \\ &= -\frac{1}{\pi^2} \mathbb{E}_{\Psi} \left[\underbrace{\int_0^{\infty} \operatorname{Im}[\phi_{\text{SINR}}(q, T_c | \Psi)] \frac{dq}{q} \int_0^{\infty} \operatorname{Im}[\phi_E^{IU}(q'; d | \Psi) e^{-jq'T_e}] \frac{dq'}{q'}}_{\Upsilon(T_c, T_e; d)} \right]. \end{aligned}$$

By applying the expectation operator, one has $\mathbb{E}_{\Psi} [F_{\text{cov}}(T_c | \Psi)] = F_{\text{cov}}(T_c)$ and $\mathbb{E}_{\Psi} [F_{\text{emfe}}^{IU}(T_e; d | \Psi)] = F_{\text{emfe}}^{IU}(T_e; d)$. due to the motion-invariance of the H-PPP in \mathbb{R}^2 , which gives the first line of Theorem 2.

B. Decomposition of $\Upsilon(T_c, T_e; d)$

The expectation over Ψ in the last expression of $\Upsilon(T_c, T_e; d)$ can be decomposed in the following manner:

$$\mathbb{E}_{\Psi} [\cdot] \rightarrow \mathbb{E}_{X_0} [\mathbb{E}_{\Psi \setminus \{X_0\}} [\cdot]]$$

where the coordinates of the serving BS X_0 are (R_0, Θ_0) . Additionally, we write $\Psi^* = \Psi \setminus \{X_0\}$. Building up on these notations and using the PDF (1), we obtain

$$\Upsilon(T_c, T_e; d) = \frac{1}{2\pi} \int_{r_e}^{\tau} \int_0^{2\pi} \Upsilon(T_c, T_e; d | r_0, \theta_0) d\theta f_{R_0}(r_0) dr_0.$$

where

$$\begin{aligned} & \Upsilon(T_c, T_e; d | R_0, \Theta_0) \\ &= \mathbb{E}_{\Psi^*} \left[\int_0^{\infty} \operatorname{Im}[\phi_I(-qT_c | \Psi) \phi_S(q; 0 | \Psi) e^{-jqT_c\sigma^2}] \frac{1}{q} dq \right. \\ & \quad \left. \times \int_0^{\infty} \operatorname{Im}[\phi_I(q' | \Psi) \phi_S(q'; d | \Psi) e^{-jq'T_e}] \frac{1}{q'} dq' \right] \end{aligned}$$

Let $v_1 = \phi_S(q; 0 | \Psi) e^{-jqT_c\sigma^2}$ and $v_2 = \phi_S(q'; d | \Psi) e^{-jq'T_e}$. By swapping the expectation and the integrals, following Fubini's theorem, we obtain

$$\begin{aligned} & \Upsilon(T_c, T_e; d | R_0, \Theta_0) \\ &= \int_0^{\infty} \int_0^{\infty} \underbrace{\mathbb{E}_{\Psi^*} [\operatorname{Im}[\phi_I(-qT_c | \Psi) v_1] \operatorname{Im}[\phi_I(q' | \Psi) v_2]]}_{\epsilon(q, q'; T_c, T_e, d | R_0, \Theta_0)} \frac{dq dq'}{q q'}. \end{aligned} \quad (41)$$

C. Decomposition of $\epsilon(q, q'; T_c, T_e, d | r_0, \theta_0)$

Since ϕ_S does not depend on Ψ^* , by using $\operatorname{Im}[x] = \frac{x-\bar{x}}{2}$ and $\operatorname{Re}[x] = \frac{x+\bar{x}}{2}$, we obtain

$$\begin{aligned} & \epsilon(q, q'; T_c, T_e, d | R_0, \Theta_0) \\ &= \frac{1}{4} \mathbb{E}_{\Psi^*} \left[(\phi_I(-qT_c | \Psi) v_1 - \bar{\phi}_I(-qT_c | \Psi) \bar{v}_1) \right. \\ & \quad \left. \times (\phi_I(q' | \Psi) v_2 - \bar{\phi}_I(q' | \Psi) \bar{v}_2) \right] \\ &= \frac{1}{4} \mathbb{E}_{\Psi^*} [\phi_I(-qT_c | \Psi) \phi_I(q' | \Psi)] v_1 v_2 \\ & \quad - \frac{1}{4} \mathbb{E}_{\Psi^*} [\phi_I(-qT_c | \Psi) \bar{\phi}_I(q' | \Psi)] v_1 \bar{v}_2 \\ & \quad - \frac{1}{4} \mathbb{E}_{\Psi^*} [\bar{\phi}_I(-qT_c | \Psi) \phi_I(q' | \Psi)] \bar{v}_1 v_2 \\ & \quad + \frac{1}{4} \mathbb{E}_{\Psi^*} [\bar{\phi}_I(-qT_c | \Psi) \bar{\phi}_I(q' | \Psi)] \bar{v}_1 \bar{v}_2 \\ &= \frac{1}{2} \operatorname{Re}[\gamma_+(q, q' | r_0) v_1 v_2] - \frac{1}{2} \operatorname{Re}[\gamma_-(q, q' | r_0) v_1 \bar{v}_2] \end{aligned} \quad (42)$$

where we define $\gamma_+(q, q' | r_0) = \mathbb{E}_{\Psi^*} [\phi_I(q | \Psi) \phi_I(q' | \Psi)]$ and $\gamma_-(q, q' | r_0) = \mathbb{E}_{\Psi^*} [\phi_I(q | \Psi) \bar{\phi}_I(q' | \Psi)]$.

D. Decomposition of γ_+ and γ_-

The methodology employed to calculate the expressions of γ_+ and γ_- aligns with the approach detailed in Appendix C of [43] for the identical network pertaining to a RU. The only modification required lies in adjusting the lower bound of the integral in equation (30), substituting r_0 for r_e .

REFERENCES

- [1] M. Rumney, "5G Safety : A scientific response to an increasingly polarized debate," *COST Action CA15104: Fourth and Final Scientific Annual Report (TD(19)11003)*, 2019.
- [2] ICNIRP, "ICNIRP Guidelines for Limiting Exposure to Electromagnetic Fields (100 kHz to 300 GHz)," *Health Physics*, vol. 118, pp. 483–524, 2020.

- [3] ANFR, "Evaluation de l'exposition du public aux ondes électromagnétiques 5G Volet 1 : présentation générale de la 5G," pp. 1–17, 2019.
- [4] E. C. Strinati *et al.*, "Wireless Environment as a Service Enabled by Reconfigurable Intelligent Surfaces: The RISE-6G Perspective," in *2021 Joint European Conference on Networks and Communications & 6G Summit (EuCNC/6G Summit)*, 2021, pp. 562–567.
- [5] S. Aerts, L. Verloock, M. Van den Bossche, and J. Wout, "In-situ metingen van radiofrequente elektromagnetische velden in de nabijheid van een 5G NR-basisstation," IMEC - WAVES - Ghent University, Tech. Rep., March 2020.
- [6] G. Vermeeren *et al.*, "Low EMF exposure future networks D2. 8 global wireless exposure metric definition," LEXNET Consortium, Tech. Rep., 2015.
- [7] S. Aerts *et al.*, "In-situ Measurement Methodology for the Assessment of 5G NR Massive MIMO Base Station Exposure at Sub-6 GHz Frequencies," *IEEE Access*, vol. 7, pp. 184 658–184 667, 2019.
- [8] "Study of the contribution of 5G to the general public exposure to electromagnetic waves," Agence Nationale des Fréquences, Tech. Rep., 2021.
- [9] L. Chiaraviglio, S. Rossetti, S. Saida, S. Bartoletti, and N. Blefari-Melazzi, "Pencil Beamforming Increases Human Exposure to ElectroMagnetic Fields": True or False?" *IEEE Access*, vol. 9, pp. 25 158–25 171, 2021.
- [10] M. S. Elbasheir *et al.*, "A Review of EMF Radiation for 5G Mobile Communication Systems," in *2021 IEEE Asia-Pacific Conference on Applied Electromagnetics (APACE)*, 2021, pp. 1–6.
- [11] I. Patsouras *et al.*, "Beyond 5G/6G EMF Considerations," Jul. 2023. [Online]. Available: <https://doi.org/10.5281/zenodo.8099834>
- [12] H. B. A. Sidi and Z. Altman, "Small Cells' Deployment Strategy and Self-Optimization for EMF Exposure Reduction in HetNets," *IEEE Transactions on Vehicular Technology*, vol. 65, no. 9, pp. 7184–7194, 2015.
- [13] A. T. Ajibare, D. Ramotsoela, L. A. Akinyemi, and S. O. Oladejo, "RF EMF Radiation Exposure Assessment of 5G Networks: Analysis, Computation and Mitigation Methods," in *2021 IEEE AFRICON*, 2021, pp. 1–6.
- [14] E. C. Strinati *et al.*, "Reconfigurable, Intelligent, and Sustainable Wireless Environments for 6G Smart Connectivity," *IEEE Communications Magazine*, vol. 59, no. 10, pp. 99–105, 2021.
- [15] D.-T. Phan-Huy, Y. Bénédict, S. H. Gonzalez, and P. Ratajczak, "Creating and Operating Areas With Reduced Electromagnetic Field Exposure Thanks to Reconfigurable Intelligent Surfaces," in *2022 IEEE 23rd International Workshop on Signal Processing Advances in Wireless Communication (SPAWC)*, 2022, pp. 1–5.
- [16] H. Ibraiwish, A. Elzanaty, Y. H. Al-Badarnah, and M.-S. Alouini, "EMF-Aware Cellular Networks in RIS-Assisted Environments," *IEEE Communications Letters*, vol. 26, no. 1, pp. 123–127, 2022.
- [17] F. Baccelli, M. Klein, M. Lebourges, and S. A. Zuyev, "Stochastic geometry and architecture of communication networks," *Telecommunication Systems*, vol. 7, pp. 209–227, 1997.
- [18] C.-H. Lee, C.-Y. Shih, and Y.-S. Chen, "Stochastic Geometry Based Models for Modeling Cellular Networks in Urban Areas," *Wirel. Netw.*, vol. 19, no. 6, p. 1063–1072, aug 2013.
- [19] D. Maamari, N. Devroye, and D. Tuninetti, "Coverage in mmWave Cellular Networks With Base Station Co-Operation," *IEEE Transactions on Wireless Communications*, vol. 15, no. 4, pp. 2981–2994, 2016.
- [20] X. Yu, J. Zhang, M. Haenggi, and K. B. Letaief, "Coverage Analysis for Millimeter Wave Networks: The Impact of Directional Antenna Arrays," *IEEE Journal on Selected Areas in Communications*, vol. 35, no. 7, pp. 1498–1512, 2017.
- [21] M. Di Renzo, "Stochastic Geometry Modeling and Analysis of Multi-Tier Millimeter Wave Cellular Networks," *IEEE Transactions on Wireless Communications*, vol. 14, no. 9, pp. 5038–5057, 2015.
- [22] S. S. Kalamkar, F. Baccelli, F. M. Abinader, A. S. M. Fani, and L. G. U. Garcia, "Beam Management in 5G: A Stochastic Geometry Analysis," *IEEE Transactions on Wireless Communications*, vol. 21, no. 4, pp. 2275–2290, 2022.
- [23] N. A. Muhammad, N. Seman, and N. I. A. Apandi, "Effect of Directional Antenna Arrays on Millimeter Wave Cellular Networks," in *2022 International Symposium on Antennas and Propagation (ISAP)*, 2022, pp. 205–206.
- [24] Y. Nabil, H. ElSawy, S. Al-Dharrab, H. Attia, and H. Mostafa, "A Stochastic Geometry Analysis for Joint Radar Communication System in Millimeter-wave Band," in *ICC 2023 - IEEE International Conference on Communications*, 2023, pp. 5849–5854.
- [25] A. Thornburg and R. W. Heath, "Ergodic capacity in mmWave ad hoc network with imperfect beam alignment," in *MILCOM 2015 - 2015 IEEE Military Communications Conference*, 2015, pp. 1479–1484.
- [26] M. Rebato, J. Park, P. Popovski, E. De Carvalho, and M. Zorzi, "Stochastic Geometric Coverage Analysis in mmWave Cellular Networks With Realistic Channel and Antenna Radiation Models," *IEEE Transactions on Communications*, vol. 67, no. 5, pp. 3736–3752, 2019.
- [27] R. Aghazadeh Ayoubi and U. Spagnolini, "Performance of Dense Wireless Networks in 5G and beyond Using Stochastic Geometry," *Mathematics*, vol. 10, no. 7, 2022. [Online]. Available: <https://www.mdpi.com/2227-7390/10/7/1156>
- [28] T. A. Khan, A. Alkhateeb, and R. W. Heath, "Millimeter Wave Energy Harvesting," *IEEE Transactions on Wireless Communications*, vol. 15, no. 9, pp. 6048–6062, 2016.
- [29] J. Guo, X. Zhou, and S. Durrani, "Wireless Power Transfer via mmWave Power Beacons With Directional Beamforming," *IEEE Wireless Communications Letters*, vol. 8, no. 1, pp. 17–20, 2019.
- [30] N. Deng and M. Haenggi, "Energy Correlation Coefficient in Wirelessly Powered Networks with Energy Beamforming," in *ICC 2021 - IEEE International Conference on Communications*, 2021, pp. 1–6.
- [31] M. Di Renzo and W. Lu, "System-Level Analysis and Optimization of Cellular Networks With Simultaneous Wireless Information and Power Transfer: Stochastic Geometry Modeling," *IEEE Transactions on Vehicular Technology*, vol. 66, no. 3, pp. 2251–2275, 2017.
- [32] T. Tu Lam, M. Di Renzo, and J. P. Coon, "System-Level Analysis of SWIPT MIMO Cellular Networks," *IEEE Communications Letters*, vol. 20, no. 10, pp. 2011–2014, 2016.
- [33] M. Wang, C. Zhang, X. Chen, and S. Tang, "Performance Analysis of Millimeter Wave Wireless Power Transfer With Imperfect Beam Alignment," *IEEE Transactions on Vehicular Technology*, vol. 70, no. 3, pp. 2605–2618, 2021.
- [34] M. Al Hajj, S. Wang, L. Thanh Tu, S. Azzi, and J. Wiat, "A Statistical Estimation of 5G Massive MIMO Networks' Exposure Using Stochastic Geometry in mmWave Bands," *Applied Sciences*, vol. 10, no. 23, 2020.
- [35] Q. Gontier, L. Petrillo, F. Rottenberg, F. Horlin, J. Wiat, C. Oestges, and P. De Doncker, "A Stochastic Geometry Approach to EMF Exposure Modeling," *IEEE Access*, vol. 9, pp. 91 777–91 787, 2021.
- [36] M. A. Hajj, S. Wang, and J. Wiat, "Characterization of EMF Exposure in Massive MIMO Antenna Networks with Max-Min Fairness Power Control," in *2022 16th European Conference on Antennas and Propagation (EuCAP)*, 2022, pp. 1–5.
- [37] N. A. Muhammad *et al.*, "Stochastic Geometry Analysis of Electromagnetic Field Exposure in Coexisting Sub-6 GHz and Millimeter Wave Networks," *IEEE Access*, vol. 9, pp. 112 780–112 791, 2021.
- [38] Q. Gontier *et al.*, "Joint Metrics for EMF Exposure and Coverage in Real-World Homogeneous and Inhomogeneous Cellular Networks," *IEEE Transactions on Wireless Communications*, pp. 1–1, 2024.
- [39] C. Wiame, S. Demey, L. Vandendorpe, P. De Doncker, and C. Oestges, "Joint Data Rate and EMF Exposure Analysis in Manhattan Environments: Stochastic Geometry and Ray Tracing Approaches," *IEEE Transactions on Vehicular Technology*, vol. 73, no. 1, pp. 894–908, 2024.
- [40] C. Wiame, C. Oestges, and L. Vandendorpe, "Joint data rate and EMF exposure analysis in user-centric cell-free massive MIMO networks," 2023, submitted. [Online]. Available: <https://arxiv.org/abs/2301.11127>
- [41] Q. Gontier *et al.*, "On the Uplink and Downlink EMF Exposure and Coverage in Dense Cellular Networks: A Stochastic Geometry Approach," 2024, submitted. [Online]. Available: <https://arxiv.org/abs/2312.08978>
- [42] L. Chen, A. Elzanaty, M. A. Kishk, L. Chiaraviglio, and M.-S. Alouini, "Joint Uplink and Downlink EMF Exposure: Performance Analysis and Design Insights," *IEEE Transactions on Wireless Communications*, vol. 22, no. 10, pp. 6474–6488, 2023.
- [43] Q. Gontier *et al.*, "Meta Distribution of Passive Electromagnetic Field Exposure in Cellular Networks," 2024, unpublished. [Online]. Available: <https://arxiv.org/abs/2302.03559>
- [44] J. Gil-Pelaez, "Note on the inversion theorem," *Biometrika*, vol. 38, no. 3-4, pp. 481–482, 12 1951.
- [45] S. Ichitsubo, T. Furuno, T. Taga, and R. Kawasaki, "Multipath propagation model for line-of-sight street microcells in urban area," *IEEE Transactions on Vehicular Technology*, vol. 49, no. 2, pp. 422–427, 2000.
- [46] E. Dahlman, S. Parkvall, and J. Skold, *5G NR: The Next Generation Wireless Access Technology*, 1st ed. USA: Academic Press, Inc., 2018.
- [47] I. Gradshteyn and I. Ryzhik, "Use of the Tables," in *Table of Integrals, Series, and Products (Eighth Edition)*, D. Zwillinger, V. Moll, I. Gradshteyn, and I. Ryzhik, Eds. Boston: Academic Press, 2014, pp. xxix–xxxvi.